scientific reports

Check for updates

OPEN

Superior charge storage performance of optimized nickel cobalt carbonate hydroxide hydrate nanostructures for supercapacitor application

Mohit Bhatt[1]✉, Bhavana Gupta[2] & A. K. Sinha[1]✉

In our work, we report superior electrochemical performance of optimized 3D nanostructured, nickel-cobalt carbonate hydroxide hydrate ($Ni_{3-x}Co_x$-CHH ($1 \leq x \leq 2$)) materials with flower like morphology synthesised via one-step hydrothermal methods. A Ni rich sample ($x = 1$) demonstrate better specific capacitance and the improvement is attributed to more oxygen deficient neighbourhood of Ni compared to that of Co. The structural, morphological and electronic properties of the samples were investigated using X-ray diffraction (XRD), Fourier transform infrared spectroscopy (FTIR), High resolution transmission electron microscopy (HRTEM), field emission electron microscopy (FESEM), Energy-dispersive X-ray spectroscopy (EDX), and X-ray photoelectron spectroscopy (XPS). A comprehensive characterization was used for physicochemical properties-electrochemical performance correlation. Cyclic voltammetry (CV), Galvanostatic charging and discharging (GCD) shows the supercapacitor feature of the samples for the composition containing the highest nickel concentration achieving a specific capacitance of 1649.51 F g^{-1} at a current density of 1 A g^{-1} and excellent rate capability of 1610.30 F g^{-1} at a high current density of 5 A g^{-1}. The sample shows high cyclic stability of 80.86% after 3000 cycles. Improved specific capacitance is attributed to the synergy effect of bimetallic transition metals as well as improved surface area of flower like morphology. These findings show that Ni_2Co-CHH electrode material demonstrates great potential as electrode material for supercapacitor device fabrication.

Keywords Nickel-cobalt carbonate hydroxide hydrate, Transition metals compound, Hydrothermal synthesis, Electrochemical performance, Supercapacitor, Energy storage

Energy storage is a critical aspect of modern technological advancements, playing a pivotal role in addressing the intermittent nature of renewable energy sources, grid stability, and the burgeoning demands of portable electronics and electric vehicles[1,2]. The applications of supercapacitors (SCs) with high power density are plagued by its low energy density. A lot of efforts are directed towards attaining better energy density in supercapacitors. In this context, the development of high-performance electrode materials for energy storage applications is the most critical component for enhancing the efficiency, reliability, and sustainability of these devices[3]. Electrode materials, in particular, are crucial in determining the overall performance of various energy storage devices, such as batteries and supercapacitors, by facilitating charge storage and release processes[4,5]. Consequently, the quest for efficient and optimised electrode materials remains a vital pursuit in energy storage research, aiming to unlock higher energy densities, improved cycling stability, and enhanced electrochemical performance[6].

SCs, which rely on Faradic redox reactions for charge storage and discharge, exhibit much higher power densities and longer life cycles but generally lower energy densities compared to batteries[7,8]. Conversely, SCs offer significantly higher energy densities than conventional capacitors, whose energy storage mechanism is non-Faradic and depends on the polarisation of the dielectric material[8,9]. Based on their charge storage mechanisms, SCs are classified into two categories[10]: electric double-layer capacitors (EDLCs) and pseudocapacitors.

[1]Department of Physics, School of Advanced Engineering, UPES, Dehradun, India. [2]Department of Chemistry, School of Advanced Engineering, UPES, Dehradun, India. ✉email: mhtt.mb@gmail.com; anilksinha11@gmail.com

In EDLCs, charge is stored at the interface between the electrode and the electrolyte, resulting in limited capacitance; materials like activated carbon and graphite are commonly used as electrodes for EDLCs [2,11]. The choice of electrode material is especially critical for pseudocapacitors and batteries, where efficient charge storage depends on reversible Faradic redox reactions between the electro- active material and the electrolyte[11,12]. This mechanism involves both surface adsorption and intercalation, necessitating electrode materials with high surface areas and structural stability[11,12]. Additionally, these materials must possess high electrical conductivity. To achieve high surface area without compromising structural integrity, various nanostructures with hierarchical pores and varied surface morphologies have been used by researcher[13,14]. Enhancing ion kinetics and optimising performance parameters such as energy and power density, life cycle, coulombic efficiency, and rate capability have been achieved through engineered surface chemistry (dopants and chemically active sites) and defect structures[9,15].

From the perspective of material, three primary classes are utilised as electrodes for SCs: (a) carbon-based materials, including activated carbon, carbon dots (0-D), carbon nanotubes (1-D), and graphene (2-D); (b) conducting polymers and their derivatives; and (c) transition metal compounds (TMCs) and their derivatives[16,17]. TMCs are particularly promising due to their high theoretical capacities and variable oxidation states, which enhance redox behaviour and electrochemical performance[18–20]. However, the use of transition metal oxides (TMOs) as electrodes in batteries and SCs is limited by their low electrical conductivity and poor cycle life, primarily due to issues like pulverisation and structural degradation during charge-discharge cycles[18,19]. While transition metal sulfides offer better electrical conductivity compared to oxides, their synthesis usually involves complex and high-temperature sulfurization processes in inert atmospheres, which can be impractical and costly[18,21].

In recent years, a variety of carbonate hydroxides have been investigated, including nickel carbonate hydroxide (NiCH)[22], nickel carbonate hydroxide hydrate (Ni-CHH), nickel copper carbonate hydroxide (NiCuCH)[23], copper cobalt carbonate hydroxide (CuCoCH)[24], graphene oxide-induced nickel cobalt carbonate hydroxide (GO/NiCoCH)[25], cobalt carbonate hydroxide (CoCH)[26,27], and nickel carbonate hydroxide/zeolitic imidazolate framework-8 (NiCH/ZIF-8)[28]. The remarkable electrochemical performance of these materials is largely attributed to the presence of hydrophilic CO_3^{2-} ions, which significantly enhance electrolyte wettability[24], rich redox reaction and its layered structure induce easy mass transfer at the electrode-electrolyte interfaces. These attributes high surface area with enhanced active site accessibility. On the negative side, the material suffers from low electronic conductivity, which leads to slow reaction kinetics and overpotentials. Nickel-based electrode materials, such as nickel oxide (NiO) and nickel hydroxide ($Ni(OH)_2$), have been extensively researched for their high theoretical specific capacity[29]. Furthermore, cobalt is known for its ability to modify morphology and enhance the conductivity of electrode materials, thereby improving their electrochemical properties. Consequently, incorporating cobalt into nickel carbonate hydroxide is anticipated to significantly boost its electrochemical performance[30]. Mono-metal materials like nickel carbonate hydroxide hydrate (Ni-CHH) stand out due to their unique flower-like nanostructures and hierarchical pore architecture, positioning them as promising electrode materials for SCs[31]. The flower-like morphology of Ni-CHH not only facilitates efficient charge transport but also enhances redox behaviour due to the variable oxidation states of nickel, leading to superior electrochemical performance. The presence of hydroxide groups in Ni-CHH provides additional active sites for redox reactions, further enhancing electrochemical activity and structural stability during charge-discharge cycles. These features make Ni-CHH a viable candidate for high-performance energy storage applications, potentially overcoming the limitations of traditional transition metal oxides (TMOs). Similarly, cobalt carbonate hydroxide (Co-CHH) has been evaluated as an electrode material, exhibiting benefits such as improved charge transport and electrochemical activity due to its unique morphology and multiple oxidation states that facilitate efficient redox reactions. Co-CHH has demonstrated promising electrochemical performance[32].

Bimetallic transition metal compounds, particularly those involving nickel and cobalt, have shown superior electrochemical performance compared to their monometallic counterparts[33]. For example, $CoNi_2O_4$ exhibits electrical conductivity that is orders of magnitude higher than either cobalt or nickel oxides alone[34], an improvement often attributed to self-doping effects. Our recent studies on the electronic properties of nickel, cobalt, and bimetallic CHH using X-ray Absorption Near Edge Structure (XANES) and Soft X-ray Absorption Spectroscopy (XAS) revealed that in bimetallic CHH samples, nickel exhibits an oxidation state lower than +2, while cobalt shows an oxidation state of +2. The presence of oxygen-deficient nickel sites likely enhances electrochemical properties[35]. Literature reports indicate that Nickel-CHH nanostructures exhibit notable specific capacitance, such as 353 mAh g^{-1} at 1 mV s^{-1} and 245 mAh g^{-1} at a current density of 1.83 A g^{-1}[31].

By combining unique features of bimetallic redox synergy and carbonate hydroxide hydrate charge stabilizing, our research demonstrates improved electrochemical performance for bimetallic Ni_2CoCHH with optimum Ni and Co concentration i.e. 2:1. The electrode material have shown a high specific capacitance and excellent rate capability event at high current density. Using a straightforward one-step hydrothermal synthesis method, we successfully prepared hierarchical, flower-like spherical Ni_2Co-CHH materials for advanced SCs applications. The specific capacitance of the synthesised Ni_2Co-CHH demonstrated good cycling stability and prolonged performance, highlighting the potential of Ni_2Co-CHH nanostructure as high-performance electrode materials for SCs.

Experimental section

Materials

Nickel (II) nitrate hexahydrate ($Ni(NO_3)_2.6H_2O$, cobalt (II) nitrate hexahydrate ($Co(NO_3)_2.6H_2O$),) Urea (NH_2CONH_2), double deionized water, ethanol, acetone and Hydrochloric acid (HCl).

Synthesis and growth mechanism of Ni3 – xCox-CHH ($1 \leq x \leq 2$)

$Ni_{3-x}Co_x$-CHH material was synthesized via a one-step hydrothermal synthesis method, optimized by varying the concentrations of nickel and cobalt salt in ratios of 1:2, 2:1, and 1:1 while keeping other constituent in same concentration[31]. For the preparation of $NiCo_2$-CHH material, 4 mmol of nickel nitrate hexahydrate ($Ni(NO_3)_2.6H_2O$), 8 mmol of cobalt nitrate hexahydrate ($Co(NO_3)_2.6H_2O$), and 12 mmol of urea (NH_2CONH_2) were dissolved in 60 mL of deionised water and stirred for 30 min to form a light pink solution. We prepared four pieces of nickel foam (NF) with dimensions of 1 cm × 1 cm × 0.5 cm, which were used as the conducting surface/substrate for the material. These NF pieces were cleaned using acetone, ethanol, and diluted acid with bath sonication. Cleaning nickel foam removes contaminants like, dust particle, and chemical residues, ensuring better adhesion and uniform coating of $Ni_{3-X}Co_x$-CHH, which enhanced electrochemical activity and conductivity, improves electrical contact for better charge transfer, and reduces unwanted side reactions, thereby improving electrode performance. This solution along with cleaned NF was then transferred to a 100 mL Teflon-lined stainless-steel autoclave, sealed, and subjected to hydrothermal treatment at 120 °C for 6 h in a hot air oven. After cooling to room temperature, the resulting precipitate was thoroughly washed with ethanol and double deionised water, followed by drying overnight in a vacuum oven at 50 °C. The schematic of the synthesis process is illustrated in Fig. 1, the sequence from precursor mixing to final material drying.

The growth mechanism of $Ni_{3-X}Co_x$-CHH involves several critical steps influenced by the hydrothermal conditions and precursor ratios. We employed hydrothermal synthesis method because it offers distinct advantages in morphology control via self-assembly, making it an efficient approach for producing hierarchical porous materials with outstanding electrochemical properties. During hydrothermal synthesis, the dissolved metal nitrates undergo complexation with urea in aqueous solution, leading to the formation of metal hydroxide precursors. These precursors nucleate and grow on the surface of the NF substrate, facilitated by the controlled temperature and pressure conditions inside the autoclave. The variation in nickel and cobalt concentrations in the precursor solution impacts the stoichiometry and morphology of the resulting $Ni_{3-X}Co_x$-CHH material. Higher nickel concentrations tend to promote the formation of flower-like hierarchical structures, while cobalt-rich compositions contribute to denser nanostructures with improved electrochemical properties[36,37]. The washing steps post-hydrothermal treatment remove residual salts and impurities, ensuring the purity and stability of the final $Ni_{3-X}Co_x$-CHH material. The finally synthesized materials are three types i.e. $NiCo_2$CHH (S-01), Ni_2CoCHH (S-02), $Ni_{1.5}Co_{1.5}$CHH (S-03).

In this hydrothermal process, urea serves as a source of both carbonate and hydroxyl ions. Under these conditions, the possible chemical reactions can be outlined as follows:

$$NH_2CONH_2 + 3H_2O = 2NH_4^+ + CO_2 + 2OH^- \quad (1)$$

$$CO_2 + 2OH^- = CO_3^{2-} + H_2O \quad (2)$$

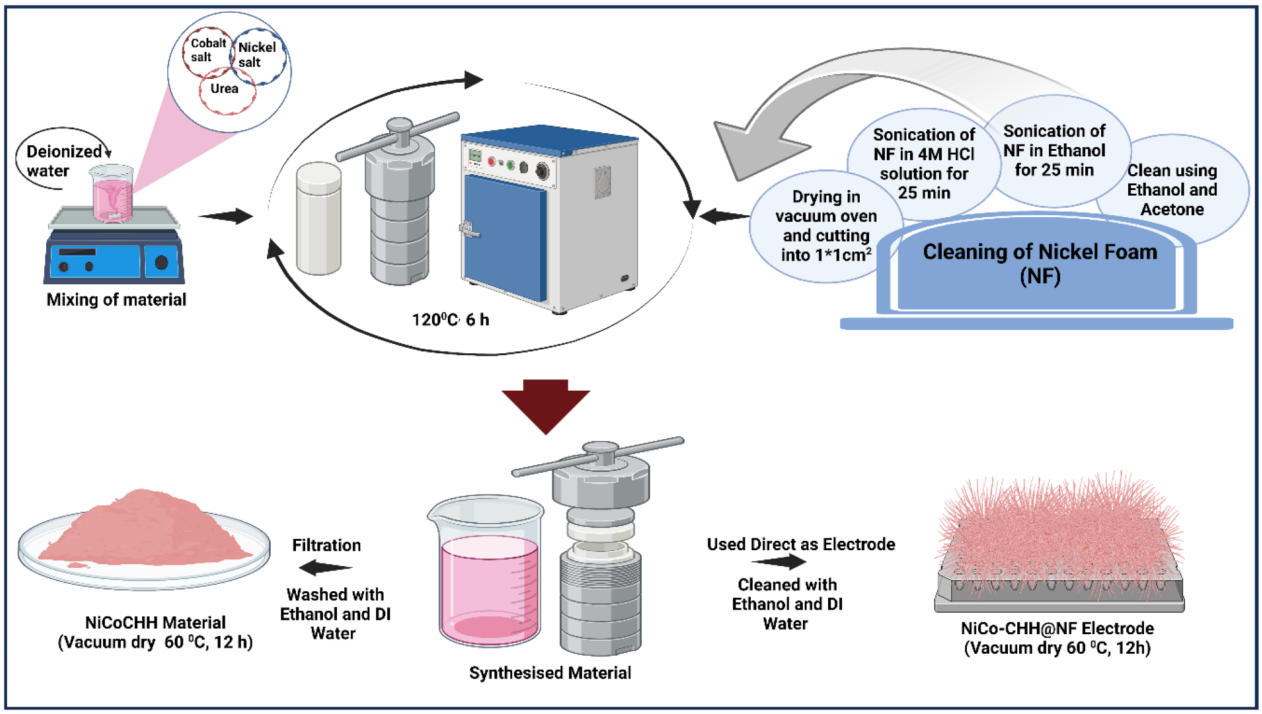

Fig. 1. Schematic diagram of procedures for preparation of Nickel cobalt carbonate hydroxide hydrate nanomaterials (Created with Biorender.com).

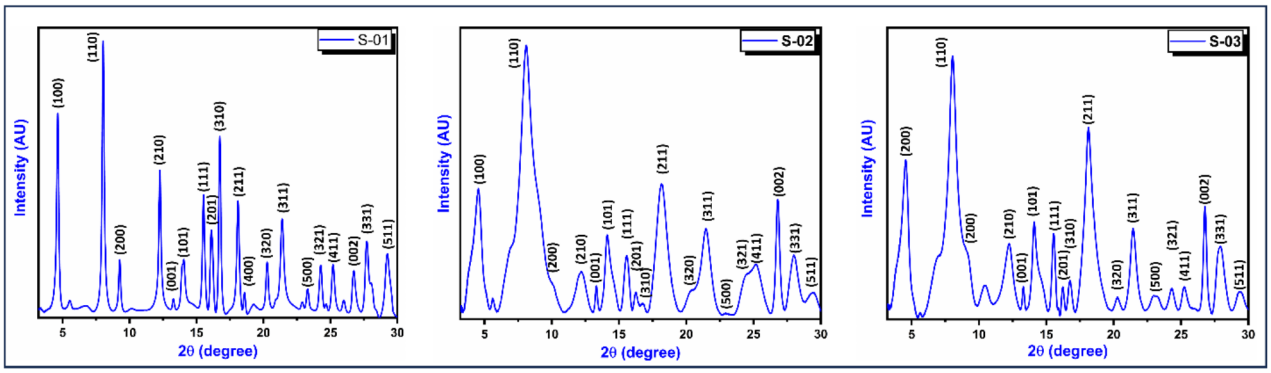

Fig. 2. XRD patterns of S-01, S-02, S-03 samples in powder form.

Materials	Lattice parameters	Crystallite size
$NiCo_2CHH$ (S-01)	a = b = 10.2410; c = 3.112 Å α = β = 90°; γ = 120°	20 ± 1
Ni_2CoCHH (S-02)	a = b = 10.4462; c = 3.1013 Å α = β = 90°; γ = 120°	9 ± 1
$Ni_{1.5}Co_{1.5}CHH$ (S-03)	a = b = 10.4361; c = 3.1048 Å α = β = 90°; γ = 120°	11 ± 1

Table 1. Lattice parameters of S-01, S-02, S-03 samples obtained from XRD results.

$$2Ni^{2+} + CO_3^{2-} + 2OH^- = Ni_2CO_3(OH)_2 \quad (3)$$

$$2CO^{2+} + CO_3^{2-} + 2OH^- = Co_2CO_3(OH)_2 \quad (4)$$

Using Eqs. 1–4, we get following possible reaction and formation of material:
$(3\text{-}x)Ni^{2+} + xCo^{2+} + (2y\text{-}1)CO_3^{2-} + yOH^- = Ni_{3-x}Co_x(CO_3)_{2y-1}(OH)_y$ (Here: $1 \le x \le 2$ $1 \le y \le 1.5$)

Sample characterisation

The examination of the NiCo-CHH material involved a thorough assessment of its morphological and structural characteristics, utilising a range of characterisation techniques. Synchrotron X-ray Diffraction (S-XRD) and Field Emission Scanning Electron Microscopy (FESEM) techniques were utilised for the structural and morphological characterisation of electrode nanomaterials, respectively. S-XRD measurements were conducted in transmission mode using an Image plate area detector (MAR 345 dtb), at a wavelength of 0.7187 Å on ADXRD beam-line (BL-12) at RRCAT-Indore, India. The FESEM analysis was carried out using a JEOL (model –JSM 7610 F Plus). Electrochemical measurements were conducted with a Biologic instrument (model-VSP-128). Fourier Transform Infrared Spectroscopy (FTIR) analysis was carried out on ParkinElmer Frontier FTIR set-up and X-ray Photoelectron Spectroscopy (XPS) was carried out using a Thermofisher scientific instrument (model – ESCALAB). These techniques offered a comprehensive understanding of the elemental composition, and chemical states present on the surface of the electrode material, adding an essential dimension to the characterization of material. In addition, electrochemical measurements (EC), includes cyclic voltammetry (CV), Galvanostatic charge-discharge (GCD), and electrochemical impedance spectroscopy (EIS), were performed to get valuable insights into the electrochemical performance of the electrode material.

Electrochemical setup

EC measurements were performed using a standard three-electrode system connected to a Biologic (model VMP-128) electrochemical workstation. The synthesised electrode material was employed as a working electrode (1×1 cm² area) and 3.6 mg mass was loaded, Pt wire mesh was used as a counter electrode, and a calomel Hg/Hg_2Cl_2 as a reference electrode. The evaluation of electrochemical performance was facilitated through three key measurements, CV, GCD and EIS. All measurements were performed in a 1 M-KOH electrolyte solution.

Results and discussion

X-ray diffraction (XRD) patterns of all the three samples (S-01, S-02, and S-03) are shown in Fig. 2 The obtained XRD patterns for all three samples exhibited multiple peaks corresponding to various crystal planes. The planes have been indexed and denotes P-62 m space group[35]. The material with a Ni: Co ratio of 1:2 (sample S-01) exhibited sharper diffraction peaks as compared to the other two samples, suggesting larger crystallite size for this sample in comparison to the other samples. The crystallite size for all three samples (S-01, S-02, and S-03) were calculated using Scherrer's formula (Eq. 1) and values along with lattice parameter are shown in Table 1.[38].

$$D = \frac{0.94\lambda}{\beta\, cos\theta} \quad (1)$$

Where, D denotes crystalline size, λ is wavelength (0.719 Å), β is full width half maxima of peaks, and θ is Braggs angle of XRD peaks. We find that the crystallite size decreases with the decrease in Ni concentration in the sample. Based on $L_{2,3}$ edge and K-edge absorption spectroscopy, we find that the oxidation state for Ni in these samples is slightly less than +2, whereas Co is in +2 oxidation state[35]. This indicates that oxygen deficient sites are concentrated on Ni sites. This may be the reason for smaller crystallite sizes in Ni rich samples.

Figure 3(1) presents the FESEM and HRTEM images, along with EDX analysis for sample S-02. Additionally, FESEM images of all samples are provided at the same resolution, showcasing two different magnifications (20,000× and 10,000×). The high magnification FESEM images confirm homogeneous flower-like morphology of the material deposited on the cage like structure of NF as shown in Fig. 3(1.b-d), clearly defining the petals and near spherical outline of the flowers. The morphology indicates high surface area and hierarchy of length scales corresponding to the petals and the outlines. It has been observed that minor instances of aggregation were present in the sample. The agglomeration can significantly impact the surface area of material, which can affect performance of material. In the context of electrode materials, agglomeration can lead to reduced surface area and hinder the efficient transport of ions and compromise on the kinetics of material and charge storage capabilities[39,40]. Furthermore, agglomerates may create localised stress points, affecting the mechanical stability of the electrode material and potentially leading to structural degradation over time. The irregular distribution of agglomerates can also cause non-uniform reactions, limiting the overall electrochemical performance[41]. From Fig. 3(2), the comparison of FESEM images reveals that samples S-01 and S-03 exhibit a closed petal flower structure, while sample S-02 presents an open flower-like structure. The lower nickel concentration in samples S-01 and S-03 indicates evidence of agglomeration, which is responsible for diminishing performance. The superiority of homogeneity and increased surface area over agglomeration underscores the promising implications of these materials for electrode fabrication in energy storage applications.

This unique morphology of S-02 provides a higher surface area, which is beneficial for accommodating more ions during charge and discharge processes. This enhanced surface area can contribute to better energy storage performance and suitable ion transport kinetics, making the material well-suited for applications like batteries and super-capacitors. Each flower of the materials is the self-assembly of several nano dimensional petals, which is clearly observed in HRTEM images after making the dispersion of the material in an appropriate solvent (Fig. 3(1.e)). Petals of the flower-like structure exhibit an approximate average width of 6 nm and length of 65 nm. This unique morphology enhances ion absorption, providing a large surface area for the Ni_2Co-CHH material. Additionally, it facilitates faster ion diffusion and shorter transport pathways within the electrode material, leading to improved overall electrochemical efficiency. Thus, the morphology and particle size revealed by the FESEM and HRTEM analyses demonstrate the potential of material as a high-performance electrode for SCs applications. The Energy Dispersive X-ray Spectroscopy (EDX) analysis for all samples is presented in Fig. 3(2). For sample S-02, we identified the elements present in the material. Although precise quantification via EDX can be challenging, the estimated composition is approximately 43 atomic % nickel (Ni) and 22 atomic % cobalt (Co), which aligns closely with the nominal Ni: Co ratio of 2:1. In sample S-03, the EDX results indicate an estimated composition of 29.5 atomic % Ni, 26.2 atomic % Co, 33.2 atomic % oxygen (O), and 11.2 atomic % carbon (C). For sample S-01, the estimated composition includes 17.9 atomic % Ni, 40.5 atomic % Co, 27.4 atomic % O, and 14.1 atomic % C.

The FTIR spectra of the three samples (S-01, S-02, and S-03) are shown in Fig. 4. The FTIR spectra provide valuable insights into the chemical composition and structural characteristics of these materials. A notable finding from these spectra is the remarkable resemblance in the infrared absorption peaks among all three samples. This uniformity strongly suggests the presence of a common functional groups hold by the samples. Three major absorption bands (~3400 cm^{-1}, ~1400 cm^{-1} and ~750 cm^{-1}) and some minor absorption peaks are observed, for all the samples. The major bands contain multiple absorption peaks. The following absorption peaks are obtained for the samples: 3524, 3410, 3082, 3289, 2792, 1472, 1378, 1071, 968, 834, 761, 697, 606, 528 and 440 cm^{-1}.The positions of most of these peaks are in very good agreement with the position of FTIR peaks in the mineral Zaratite[42].

However, the peaks have not been assigned with functional groups, in literature. Here, band around 3400 cm^{-1} is assigned to O-H stretching mode of $CO_3^-.H_2O$ (3524 cm^{-1} and 3410 cm^{-1}) and $(CO_3)^{2-}.H_2O$ (3289 cm^{-1} and 3082 cm^{-1})[43]. A major band around 3400 cm^{-1}, in our samples confirm H_2O is attached to CO_3 radical. The same band is also observed in $Ni(OH)_2$ and is ascribed to the O-H stretching mode[44]. Absorption band around 1400 cm^{-1} (1472 and 1380 cm^{-1}) is assigned to asymmetric stretching vibrations of carbonate anions[45], whereas, 697 cm^{-1} and 440 cm^{-1} peaks are attributed to TM-O stretching modes[46]. Other absorption bands below 1000 cm^{-1} are attributed to the TM-O stretching and TM-O-H bending modes[47]. From FTIR analysis, TM^{2+}, CO^{3-}, CO^{2-}, and OH radicals are confirmed in the samples.

We performed X-ray photoelectron spectroscopy (XPS) for the analysis of surface composition and valence states of the Ni_2Co-CHH samples. In Fig. 5(a), the survey XPS scan of the sample S-01 confirms the presence of carbon (C), Oxygen (O), nickel (Ni) and cobalt (Co), in the sample. Figure 5(b) shows the high-resolution spectrum of the C 1s absorption with the peaks at binding energy values of 283.8 eV, 285.5 eV corresponding to C – O, C – OH bonds, respectively. A peak corresponding to the binding energy 288.3 eV attributed to the satellite peak. The binding energy values agrees well (within 0.1 eV) to the values reported by Karthick et al.[48]. In Fig. 5(c), shows high-resolution spectra of the O 1s orbital displayed distinct peaks at binding energies of 529.8 eV, 530.5 eV, 531.4 eV, and 532.3 eV, indicating the presence of oxygen functionalities in the –OH (529.8 eV) and CO_3 (530.5 eV) groups, along with the satellite peaks[49] .

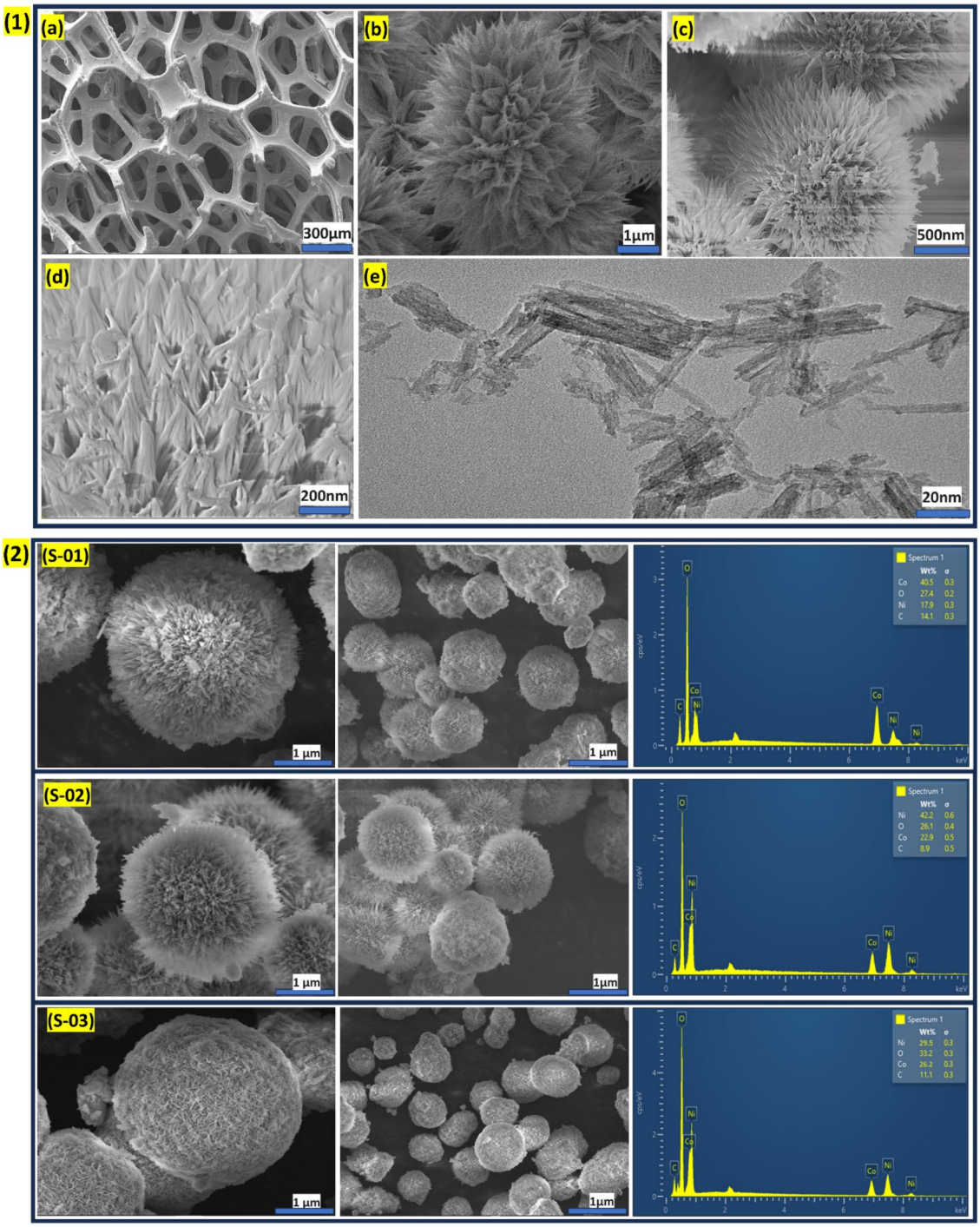

Fig. 3. (1) In-depth analysis of sample S-02, showing its detailed surface morphology and structural characteristics at various magnifications and (f) High-resolution TEM image of sample S-02, providing insight into the nanostructure and crystallinity of the material. (2) Comparison of the three samples at the same magnification and scale, highlighting differences in morphology and structural features.

In Fig. 5(d), we present high-resolution XPS Co 2p spectrum. We observe a splitting into Co $2p_{1/2}$ and Co $2p_{3/2}$ levels due to spin-orbit coupling. Peaks at 781.1 and 796.5 eV corresponding to Co $2p_{1/2}$ and Co $2p_{3/2}$ levels, respectively along with satellites at 784.9 and 801.8 eV, matches well with the values reported by Karthick et al.[48]. The fitting peaks at binding energies of 781.4 eV and 796.2 eV are indexed to Co^{2+} oxidation state[50].

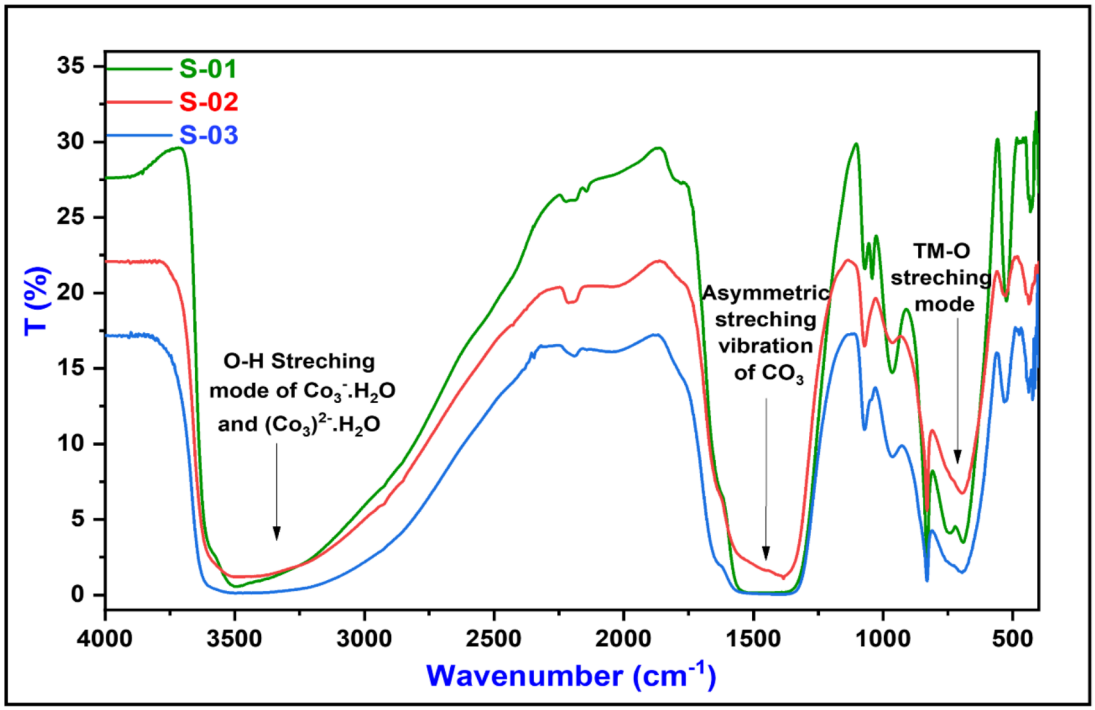

Fig. 4. FTIR spectra of S-01, S-02 and S-03 samples.

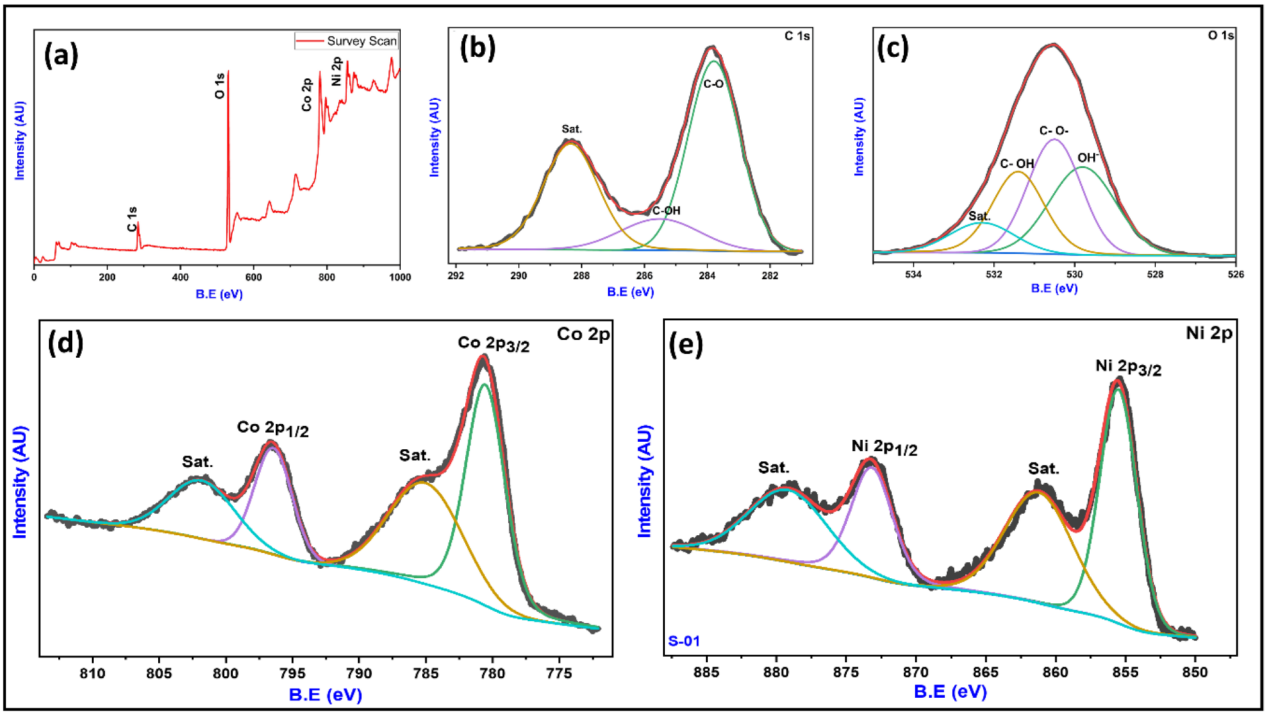

Fig. 5. (**a**) XPS survey scan of S-02 followed by deconvolution of (**b**) C 1s, (**c**) O 1s, (**d**) Co 2p, and (**e**) Ni 2p spectra.

In our material, the peaks are observed at 781.1 eV and 796.5 eV. The slight shift in binding energies indicates that the cobalt in our material is also in a similar oxidation state to Co^{2+}, but with subtle differences in the electronic environment. In Fig. 5(e), we show the detailed Ni 2p spectrum along with the fitted peaks. This spectrum also splits into Ni $2p_{1/2}$ and Ni $2p_{3/2}$ levels. The values at 855.5, 873.2, 861.2, and 879.2 eV indicates that both Ni $2p_{1/2}$ and Ni $2p_{3/2}$ peaks are blue shifted by about 1 eV compared to the peak positions reported by Karthick et al.[48], reported for bulk Ni_2CoCHH. For nickel compounds, energy difference between the mail transition peak and the satellite peak are 5.77 eV for the $2p_{3/2}$ peak and 5.68 eV for the $2p_{1/2}$.[31]. However, in our sample, the observed energy differences are 5.70 eV for the $2p_{3/2}$ peak and 6.0 eV for the $2p_{1/2}$. This slight change in the energy difference suggests material is in a slightly lower oxidation state than in the, as reported in the previous literature[31]. The changed oxidation state for Ni, therefore, indicates that Ni sites are more defective, and the defects are concentrated at Ni sites. This also justify lower crystallite size for Ni rich samples (S-02 and S-03) obtained by XRD measurements[31,50]. Additionally, it indicates that nickel is bonded to both hydroxyl and carbonate functional groups in partial oxidized state within the Ni_2Co-CHH materials[48,51]. The elemental composition of Ni_2CoCHH was assessed using XPS. XPS analysis revealed surface concentrations of 43.61% oxygen, 28.63% carbon, 8.37% nickel, and 4.28% cobalt, indicating the prevalence of surface-bound oxygen and carbon species, likely from hydroxides and carbonates group in material. In contrast, bulk composition measured via EDX revealed higher concentrations of nickel (42.2%) and cobalt (22.9%), demonstrating the difference between surface-sensitive XPS and bulk-sensitive EDX techniques. XAS data from our previous study further confirmed the electronic structure and oxidation states of the transition metals[35], showing that nickel existed in a mixed spin state with oxygen vacancies preferentially located at Ni sites, while cobalt remained in a stable low-spin state. Together with the XPS and EDX findings, these results strongly support the successful formation of the Ni_2CoCHH phase. This comprehensive analysis of both surface and bulk composition, as well as electronic structure, provides valuable insight into the characteristics of material, offering promising potential for SCs applications.

A comprehensive study using XRD, FESEM, HRTEM, FTIR, and XPS offers valuable insights into the structural, morphological, and chemical composition of $Ni_{3-x}Co_x$-CHH electrode materials, which are crucial for optimizing electrode performance. Furthermore, we performed Cyclic voltammetry (CV), Galvanostatic charging/discharging (GCD) and Electrochemical impedance spectroscopy (EIS) on all materials to evaluate their electrochemical performance. Figure 6(a) and Fig. 7(1–3.a) displays CV profiles of Ni_xCo_{3-x}-CHH@NF electrode, using a potential window ranging from −0.2 to 0.45 V. The CV scans at various scan rates for samples S-01, S-02, and S-03, as shown in Fig. 7(1–3. a), exhibit a non-rectangular shape. This suggests the faradic nature

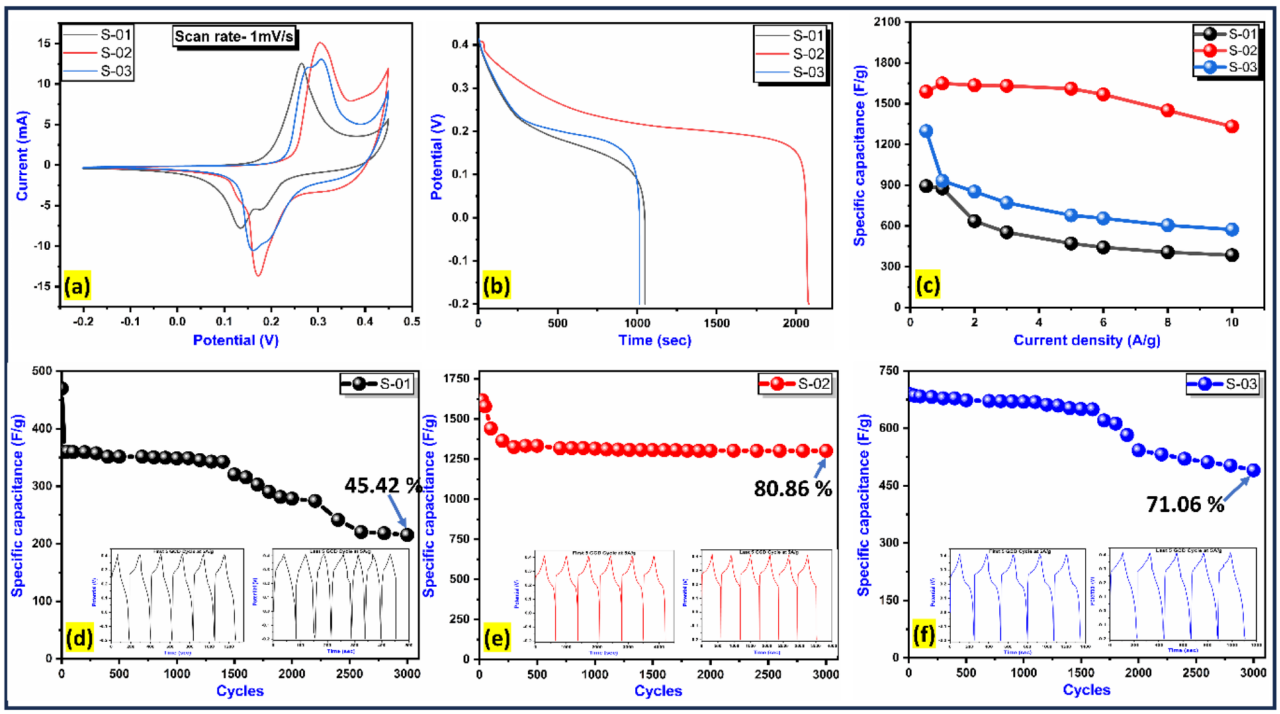

Fig. 6. (**a**) CV curves of all three samples measured at a scan rate of 1 mV/s. (**b**) GCD profiles of all three samples at a current density of 1 A/g. (**c**) Comparison for the three samples, highlighting their capacitive behaviour across varying current densities. (**d-f**) Cycling stability of the three samples, showing the specific capacitance retention over 3000 cycles at a current density of 5 A/g.

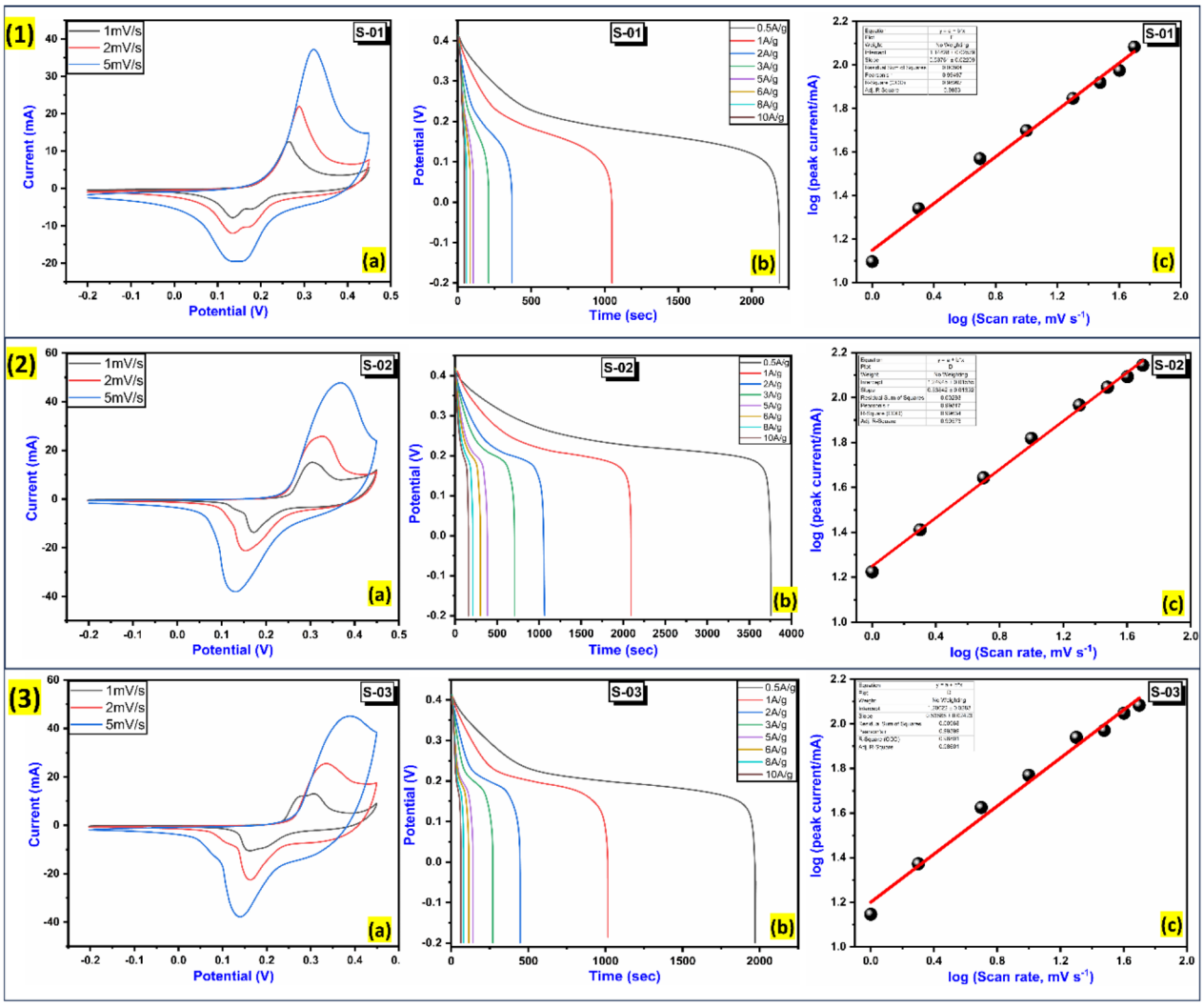

Fig. 7. 1 (**a**) Cyclic voltammetry (CV) curve, (**b**) galvanostatic charge-discharge (GCD) profile, and (**c**) anodic peak for sample S-1. 2 (**a**) Cyclic voltammetry (CV) curve, (**b**) galvanostatic charge-discharge (GCD) profile, and (**c**) anodic peak for sample S-2. 3 (**a**) Cyclic voltammetry (CV) curve, (**b**) galvanostatic charge-discharge (GCD) profile, and (**c**) anodic peak for sample S-3.

of the electrochemical reactions and indicates a battery-like redox process. Specifically for sample S-02 (Ni_2Co-CHH), distinct oxidation and reduction peaks are observed, corresponding to the Ni^{2+}/Ni^{3+} and Ni^{3+}/Ni^{2+} reversible conversion. It is proposed that, both cobalt and nickel should oxidize and reduce at the same potential. However, in samples S-01 and S-03, two closely spaced peaks appear, separated by approximately 30 mV each. Chen et al. proposed an additional step in the redox reaction of Ni-CHH, where $Ni_2(CO)(OH)_2$ converts to $Ni(OH)_2$ through the following reaction[52]:

$$Ni_2CO_3(OH)_2 + 4OH^- \rightarrow 2NiOOH + CO_3^{2-} + 2\,H_2O + 2e^-.$$

It is worth mentioning that $Ni(OH)_2$ is also an excellent battery material, and the second peak may correspond to its redox reaction.

Moreover, the area of CV curve is directly related to the electrochemically active surface area, reflecting a significant number of electroactive sites at the heterointerfaces during redox reactions[53]. The ratio of nickel to cobalt salts used in the hydrothermal synthesis plays an important role in determining the characteristics of the electrode samples. The electrode S-02 (with a Ni-to-Co ratio of 2:1) exhibits the largest CV area as compared to S-01 and S-01 at similar scan rates as shown in Fig. 6(a), suggesting it has the highest electrochemically active surface area compared to S-01 and S-03 electrode materials. In contrast, the electrode S-01 (with a Ni-to-Co ratio of 1:2) and S-03 (with a Ni-to-Co ratio of 1.5:1.5) shows the smallest CV area than S-02, indicating its inferior capacitance performance. Figure 7(1–3.a) demonstrate that increasing the scan rate enhances both the cathodic and anodic current densities.

The data reveal that the peak current is influenced by the scan rate, indicating a clear dependence of redox activity on this parameter. Interestingly, both the oxidation and reduction peaks exhibited shifts to positive and negative potentials, respectively, suggesting the quasi-reversibility of the electrode materials[54]. These results suggest that the higher nickel concentration in S-02 not only raises the oxidation potential but also contributes to improved electrochemical performance and stability of the electrode material.

Figure 7(c) Shows the behaviour of all sample (S-01, S-02 and S-03) toward the anodic peak, which was investigated using a power-law dependence Eq. 2mentionsed as following[80],

$$ip = av^b \tag{2}$$

Figure 7(c), shows anodic peak and calculated "b" value of all samples. Specifically, for Ni: Co ratios of 1:2, 2:1, and 1:1, the b values were determined to be 0.537, 0.538, 0.538, respectively. The b value serves as a crucial indicator of electrochemical behaviour, where $b = 0.5$ signifies a battery-type material and $b = 1$ denotes a capacitance-type material. Intermediate values between 0.5 and 1 ($0.5 < b < 1$) suggest a combined mechanism[37,51]. The **b** values observed for all three samples indicate a mixed battery-capacitive behaviour, with a significant capacitive component. The nearly identical "**b**" values for S-01, S-02, and S-03 (~0.538) suggest pseudo-capacitive behaviour across the samples, with a combined mechanism. The GCD profile of $Ni_{3-x}Co_x$-CHH ($1 \leq x \leq 2$) has shown in Fig. 7(b). The specific capacitance of electrode material was evaluated using following equation-3[11,37]. The measurement was done at various current densities ranging from 0.5 A g^{-1} to 10 A g^{-1}.

$$Csp = \frac{I\Delta t}{m.\Delta V} \tag{3}$$

Where, C_{sp} is the specific capacitance (F/g), I is the discharge current (Amp), Δt the discharge time (sec), ΔV the potential window (volt) and m is the active mass of the electrode material (gm).

In this study, the GCD of three samples, S-01, S-02, and S-03, was evaluated to assess their specific capacitance and stability at varying current densities. Sample S-02 exhibited an impressive specific capacitance of 1649.51 F g^{-1} at a current density of 1 A g^{-1}. Notably, at 5 A g^{-1}, the specific capacitance remained substantial at 1610.30 F g^{-1}, demonstrating a decrease of approximately 2.16% compared to its value at 1 A g^{-1}. Furthermore, at 10 A g^{-1}, S-02 maintained a high specific capacitance of 1332.08 F g^{-1}, showcasing a resilient performance with a 19.23% change from its initial value. In comparison, Sample S-01 achieved a specific capacitance of 876.39 F g^{-1} at 1 A g^{-1}, with values of 471.31 F g^{-1} at 5 A g^{-1} and 385.24 F g^{-1} at 10 A g^{-1}. Sample S-03 displayed a capacitance of 932.78 F g^{-1} at 1 A g^{-1}, decreasing to 678.50 F g^{-1} at 5 A g^{-1} and 573.77 F g^{-1} at 10 A g^{-1}. Interestingly, the stability of the materials correlates with nickel concentration, as evidenced by the performance results. Figure 6(d-f) illustrates the stability of the materials over 3000 cycles at 5 A g^{-1}. Sample S-02 displayed superior stability (Fig. 6(e)), maintaining approximately 80.86% capacitance retention, while S-03 retained 71.06% (Fig. 6(f)), and S-01 showed the least stability at 45.42% (Fig. 6(d)). These findings highlight S-02 as the best candidate for supercapacitor applications, demonstrating a robust balance between high specific capacitance and enhanced stability, consistent with our previous study[35]. Higher specific capacitance for the sample S-02, with highest nickel concentration may be due to concentration of defects and lower crystallite size of the sample. Due to the defected centre around Ni, Co electrochemical oxidation remain partial to maintain the crystal structure, while feasible and preferential oxidation of Ni helps in enhancing the energy density. The presence of oxygen-deficient defect sites in electrode was identified as particularly beneficial for charge storage through anionic charge balance. Optimum tuning of Ni and Co in $Ni_{3-X}Co_x$-CHH i.e. Ni_2CoCHH found to be superior for energy storage in comparison to many similar existing materials studied before as illustrates in Table 2. The observed trends suggest that the enhanced nickel concentration contributes significantly to the stability of the electrode materials, indicating their potential for SCs applications.

Electrochemical impedance spectroscopy (EIS) analysis of samples S-01, S-02, and S-03 was performed over a frequency range of 10 mHz to 100 kHz, as depicted in Fig. 8. The data are fitted with an equivalent circuit, shown in the left inset of Fig. 8 using EC Lab software (Biologic)[51]. The internal resistance (R_1) values for the samples S-01, S-02, and S-03 were estimated to be 0.93 Ω, 1.01 Ω, and 0.96 Ω, respectively, while their charge transfer resistance (R_2) values were 0.92 Ω, 0.74 Ω, and 0.98 Ω, respectively. Interestingly, S-02 demonstrated superior electrochemical performance among the three samples, which correlates with its significantly lower R_2. The equivalent circuit fitting revealed additional parameters for each sample. The best fit values of the capacitance (C), Warburg element (W) and the constant phase element (CPE) are given in the following Table.

Sample	R1 (Ω)	R2 (Ω)	CPE ($mF{\cdot}cm^{-2}S$)	W ($\Omega{\cdot}s^{-1/2}$)	C (mF)
S-01	0.93	0.92	4.9	10.95	1.1
S-02	1.01	0.74	10.7	13.54	3.4
S-03	0.96	0.98	7.3	12.4	1.6

The value of the fit parameters are in good agreement with published results[51]. It may be mentioned that CPE represents the non-ideal Debye behaviour. The high CPE and capacitance of S-02 reflect its superior charge storage capabilities, while its low charge transfer resistance underscores efficient charge transfer, validating its excellent conductivity and suitability for SCs applications. These findings confirm that the elemental tuning in S-02 leads to a unique morphology and outstanding electrochemical properties, solidifying its potential for future applications.

Material	Synthesis	Electrolyte	Specific capacitance	Reference
$Ni_{3-x}Co_x$-CHH ($1 \leq x \leq 2$) (S-02)	Hydrothermal	1 M KOH	1649.51 F g^{-1} at 1 A g^{-1}	In this study.
$M(CO_3)_{0.5}(OH)\cdot 0.11H_2O$	Hydrothermal	3 M KOH	9.6 mF cm^{-2} at 0.300 mA cm^{-2}	55
cobalt carbonate hydroxide hydrate (CCHH) /Polyanilines	Hydrothermal	2 M KOH	1308.4 g^{-1} at 1 A g^{-1}	49
$Co(CO_3)_{0.5}(OH)\cdot 0.11H_2O$ nanowires	Hydrothermal	2 M KOH	693.0 C g^{-1} at 1 A g^{-1}	56
$Ni_2(CO_3)(OH)_2/Co(OH)_2$	Hydrothermal	2 M KOH	632.8 C g^{-1} at 1 A g^{-1}	57
Cobalt carbonate hydroxide nanowire with nickel/cobalt MOF CCH-NCM	Hydrothermal	3 M KOH	1044.68 F g^{-1} at 2 A g^{-1}	58
$NiCuCO_3(OH)_2$	Hydrothermal	6 M KOH	971 F g^{-1} at 1 A g^{-1}	23
MnCo2O4 nanoparticles	Hydrothermal	2 M KOH	144 mF cm^{-2} at 1 A g^{-1}	59
Copper Cobalt Carbonate Hydroxides $Cu_{1.79}Co_{0.21}CH$	Hydrothermal	6 M KOH	788.9 F g^{-1}at 1 A g^{-1}	24
$Ni_2CO_3(OH)_2$	Hydrothermal	6 M KOH	668 F/g at 5 mV/s	28
Cobalt hydroxide carbonate/Activated carbon $Co_2(OH)_2CO_3$	Hydrothermal	6 M KOH	301.44 F g^{-1} at 1 A g^{-1}	60
Sea-Urchin-like Nickel–Cobalt Carbonate Hydroxide	Hydrothermal	6 M KOH	950.2 F g^{-1} at 1 A g^{-1}	37
CoV2O6 nanoparticles	Hydrothermal	----	271 mF cm^{-2} at 1 mA cm^{-2}	61
Nickel carbonate hydroxide/ zeolitic imidazolate	Hydrothermal	6 M KOH	851 F g^{-1} at 1 A g^{-1}	28
Carbon cloth @CoCH@NiCoDLH	Hydrothermal	2 M KOH	7.71 F cm^{-2} at 10 A cm^{-1}	62
Aligned nickel – cobalt hydroxide nanorod	Hydrothermal	1 M KOH	456 F g^{-1} at 20 mV/g	63
Hierarchical nanoporous nickel/nickel hydroxide structure	Hydrothermal	1 M KOH	4.76 F cm^{-1} at 6.25 mA cm^{-1}	64
Monodisperse b-phase $Co(OH)_2$ nanowires	Hydrothermal	6 M KOH	358 F g^{-1} at 0.5 A g^{-1}	65
Co_3O_4 nanotubes	Hydrothermal	6 M KOH	574 F g^{-1} at 0.1 A g^{-1}	66
$CoMoO_4$	Hydrothermal	6 M KOH	211 F g^{-1} at 0.5 A g^{-1}	67
MnCo2O4/ACWH	Hydrothermal	-----	1392 F g^{-1} at 1 A g^{-1}	68
NiFe2O4	Calcination	3 M KOH	490 F g^{-1} at 1 A g^{-1}	69
Co_3O_4 nanotubes	Hydrothermal	1 M KOH	165 F g^{-1} at 10 mV s^{-1}	70
Co_3O_4 nanowire	Hydrothermal	6 M KOH	746 F g^{-1} at 5 mA cm^{-1}	71
Graphene/Co_3O_4/polypyrrole	Hydrothermal	6 M KOH	385 F g^{-1} at 1 A g^{-1}	72
1-D) wire-like NiO/Co_3O	Hydrothermal	2 M KOH	187 F g^{-1} at 1 A g^{-1}	73
$NiCo_2O_4$ nanoparticles	Hydrothermal	2 M KOH	720.04 F g^{-1} at 1 A g^{-1}	74
Sea-urchin-like porous $NiCo_2O_4$ spinel	Hydrothermal	1 M KOH	658 F g^{-1} at 1 A g^{-1}	75
Flower-like nickel – cobalt oxides	Hydrothermal	2 M KOH	750 F g^{-1} at 1 A g^{-1}	76
Hierarchical porous nickel – cobalt oxides	Hydrothermal	2 M KOH	867.3 F g^{-1} at 1 a/g	77
FeCoP@Ni-CoCH hybrid,	Hydrothermal	2 M KOH	795.5 C g^{-1} at 1 A g^{-1}	78
Co-CHH nanostructure	Hydrothermal	3 M KOH	515 F g^{-1} at 1 mA cm^{-2}	32
$CuCoO_2$ nanostructure	Hydrothermal	2 M KOH	250 F g^{-1} at 0.5 A g^{-1}	79

Table 2. Comparative data of specific capacitance of various TMO and carbonate hydroxide materials categories synthesised via the hydrothermal route.

Conclusion

In this work, we successfully synthesised bimetallic nickel cobalt carbonate hydroxide hydrate $Ni_{3-x}Co_x$-CHH ($1 \leq x \leq 2$) nano-materials with varying Ni and Co concentrations using a simple one-step hydrothermal method. The resulting material exhibited a 3D hierarchical structure with a high surface area and flower-like morphology. HRTEM analysis confirmed that the flower petal size is ~6 nm width and ~66 nm length, which assembled in form of flower as observed in FESEM. Interestingly optimised Ni-rich samples (Ni_2Co-CHH) demonstrated smaller crystallite sizes (as confirmed by XRD) for better electrochemical performance. Electrochemical measurements revealed that the material with the highest Ni concentration (Ni_2Co-CHH) exhibited the best specific capacitance and rate performance, achieving a remarkable specific capacitance of 1649.51 F g^{-1} at current density of 1 A $g^{-1}$and 1332.08 F g^{-1} at high current density of 10 A g^{-1}. Moreover, Ni_2Co-CHH have performed superior stability, maintaining approximately 80.86% capacitance retention after 3000 cycles at 5 A g^{-1}. Thus, excellent electrochemical performance and stability can be attributed to the redox synergistic effect of bimetallic transition metals, the stable, open hierarchical structure and high porosity thus surpassing the previously reported values in literature. The hierarchical structure of electrode material significantly improved reaction kinetics and reduced material resistance, leading to outstanding specific capacitance. These findings highlight the promising potential of Ni_2Co-CHH nano-materials as electrode for supercapacitor applications.

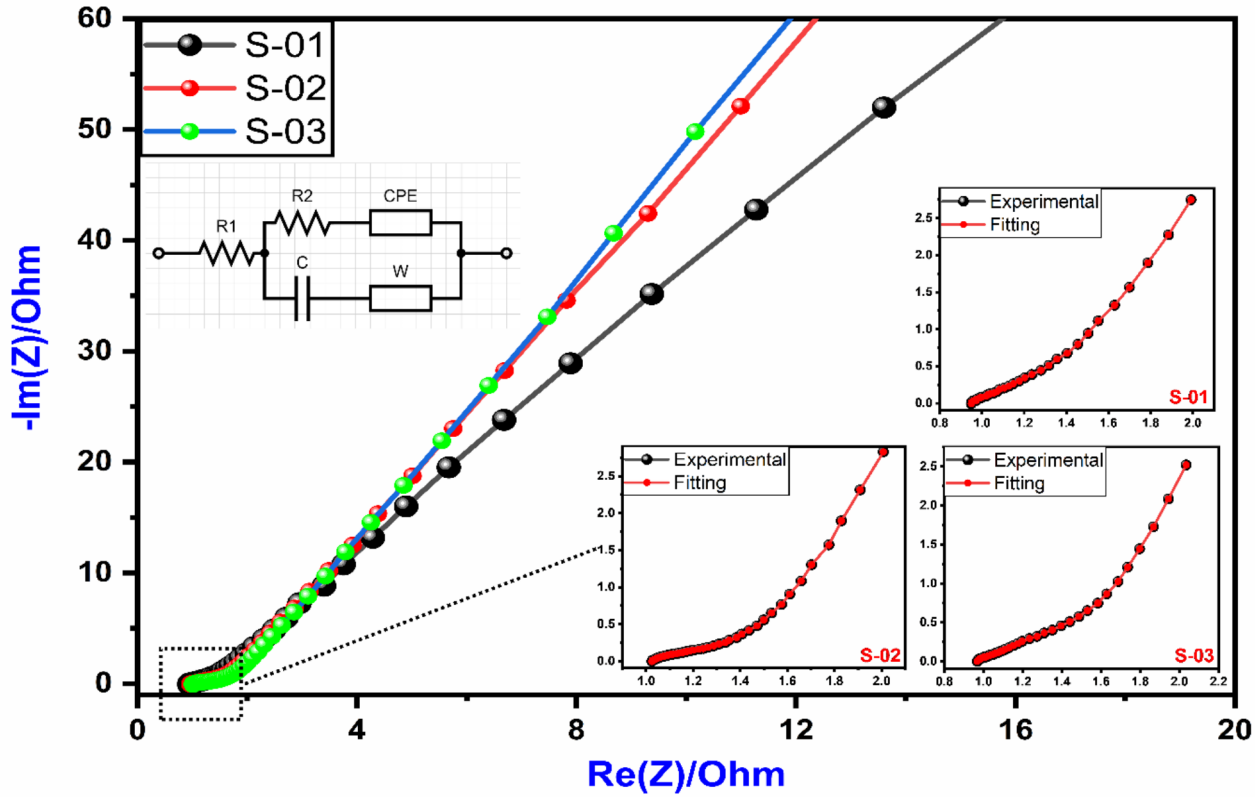

Fig. 8. EIS plot of sample S-01, S-02 and S-02.

Data availability

The datasets used and/or analysed during the current study available from the corresponding author on reasonable request.

Received: 27 July 2024; Accepted: 1 January 2025
Published online: 16 January 2025

References

1. Shelke, N. T. et al. Synthesis of Ni3V2O8-rGO composite nanostructure for high-performance hybrid supercapacitors via hydrothermal method. *Diam. Relat. Mater.* **146**, 111171 (2024).
2. Varshney, K., Varshney, P. K., Gautam, K., Tanwar, M. & Chaudhary, M. Current trends and future perspectives in the recycling of spent lead acid batteries in India. *Mater. Today Proc.* **26**, 592–602 (2020).
3. Azizi, S., Masoumnezhad, M. & Askari, M. B. Nickel ferrite oxide coated on activated carbon wheat husk for high-performance electrochemical energy storage. *Surf. Interfaces*. **40**, 103021 (2023).
4. Shaheen, I. et al. Recent advancements in metal oxides for energy storage materials: design, classification, and electrodes configuration of supercapacitor. *J. Energy Storage*. **72**, 108719 (2023).
5. Joseph, A., Perikkathra, S. & Thomas, T. Novel 2D CeO2 nanoflakes as a high-performance asymmetric supercapacitor electrode material. *J. Energy Storage*. **68**, 107757 (2023).
6. Czagany, M. et al. Supercapacitors: an efficient way for Energy Storage Application. *Materials* **17**, 702 (2024).
7. Iro, Z. S., Subramani, C. & Dash, S. S. A brief review on Electrode materials for Supercapacitor. *Int. J. Electrochem. Sci.* **11**, 10628–10643 (2016).
8. Gautham Prasad, G., Shetty, N., Thakur, S., Bommegowda, K. B. & Rakshitha & Supercapacitor technology and its applications: a review. *IOP Conf. Ser. Mater. Sci. Eng.* **561**, 012105 (2019).
9. Dubey, R. & Guruviah, V. Review of carbon-based electrode materials for supercapacitor energy storage. *Ionics* **25**, 1419–1445 (2019).
10. Yewale, M. A. et al. Elevating Supercapacitor performance of Co3O4-g-C3N4 nanocomposites fabricated via the Hydrothermal Method. *Micromachines* **15**, 414 (2024).
11. Bhojane, P. Recent advances and fundamentals of pseudocapacitors: materials, mechanism, and its understanding. *J. Energy Storage*. **45**, 103654 (2022).
12. Chen, R., Yu, M., Sahu, R. P., Puri, I. K. & Zhitomirsky, I. The development of Pseudocapacitor Electrodes and devices with high active Mass Loading. *Adv. Energy Mater.* **10**, 1903848 (2020).

13. Qin, Y. et al. Electronic structure Modulation and Phase Transformation of Nickel–Cobalt Carbonate Hydroxide caused by Halogen Doping and its effect on Supercapacitor Performance. *ACS Appl. Energy Mater.* **5**, 469–480 (2022).
14. Guo, Y., Hu, J. & Wan, L. Nanostructured materials for Electrochemical Energy Conversion and Storage Devices. *Adv. Mater.* **20**, 2878–2887 (2008).
15. Ashraf, H. & Karahan, B. D. Biowaste valorization into valuable nanomaterials: synthesis of green carbon nanodots and anode material for lithium-ion batteries from watermelon seeds. *Mater. Res. Bull.* **169**, 112492 (2024).
16. Roselin, L. S. et al. Recent advances and perspectives of Carbon-based nanostructures as Anode materials for Li-ion batteries. *Materials* **12**, 1229 (2019).
17. Ali, Z. et al. Transition metal chalcogenide anodes for sodium storage. *Mater. Today*. **35**, 131–167 (2020).
18. Pramitha, A. & Raviprakash, Y. Recent developments and viable approaches for high-performance supercapacitors using transition metal-based electrode materials. *J. Energy Storage*. **49**, 104120 (2022).
19. Sobianowska-Turek, A., Urbańska, W., Janicka, A., Zawiślak, M. & Matla, J. The Necessity of Recycling of Waste Li-Ion Batteries Used in Electric Vehicles as objects posing a threat to Human Health and the Environment. *Recycling* **6**, 35 (2021).
20. Azizi, S., Askari, M. B., Rozati, S. M. & Masoumnezhad, M. NiO/MnO_2 coated on carbon felt as an electrode material for supercapacitor applications. *Nanotechnology* **36**, 045702 (2025).
21. Khan, M. S. et al. Recent advancements in supercapacitors and their charge storage mechanism and progress in transition metal sulfide-based electrodes. *Phys. Scr.* **99**, 062001 (2024).
22. Jia, Y., Luo, T., Yu, X. Y., Liu, J. H. & Huang, X. J. Surfactant-free preparation of nickel carbonate hydroxide in aqueous solution and its toxic ion-exchange properties. *New. J. Chem.* **37**, 534–539 (2013).
23. Zheng, X., Ye, Y., Yang, Q., Geng, B. & Zhang, X. Ultrafine nickel–copper carbonate hydroxide hierarchical nanowire networks for high-performance supercapacitor electrodes. *Chem. Eng. J.* **290**, 353–360 (2016).
24. Liu, S. et al. Facile synthesis of Microsphere Copper Cobalt Carbonate Hydroxides Electrode for Asymmetric Supercapacitor. *Electrochim. Acta*. **188**, 898–908 (2016).
25. Yang, J., Yu, C., Fan, X., Zhao, C. & Qiu, J. Ultrafast Self-Assembly of Graphene Oxide-Induced monolithic NiCo–Carbonate Hydroxide Nanowire architectures with a Superior Volumetric Capacitance for Supercapacitors. *Adv. Funct. Mater.* **25**, 2109–2116 (2015).
26. Lu, Z. et al. High pseudocapacitive cobalt carbonate hydroxide films derived from CoAl layered double hydroxides. *Nanoscale* **4**, 3640 (2012).
27. Xie, H., Tang, S., Zhu, J., Vongehr, S. & Meng, X. A high energy density asymmetric all-solid-state supercapacitor based on cobalt carbonate hydroxide nanowire covered N-doped graphene and porous graphene electrodes. *J. Mater. Chem. A*. **3**, 18505–18513 (2015).
28. Gao, Y. et al. Synthesis of nickel carbonate hydroxide/zeolitic imidazolate framework-8 as a supercapacitors electrode. *RSC Adv.* **4**, 36366–36371 (2014).
29. Li, B., Zheng, M., Xue, H. & Pang, H. High performance electrochemical capacitor materials focusing on nickel based materials. *Inorg. Chem. Front.* **3**, 175–202 (2016).
30. Li, Y. L. et al. Preparation of Nickel-Cobalt Layered double hydroxides for the battery-like electrodes in Rotor–Stator Reactor. *Int. J. Electrochem. Sci.* **12**, 3432–3442 (2017).
31. Bhojane, P., Sinha, L., Goutam, U. K. & Shirage, P. M. A 3D mesoporous flowers of nickel carbonate hydroxide hydrate for high-performance electrochemical energy storage application. *Electrochim. Acta*. **296**, 112–119 (2019).
32. Pugalenthiyar, T. et al. Two-Dimensional Synergistic Interfacial Orientation on Tin Oxide-Reinforced Cobalt Carbonate Hydroxide heterostructures for High-Performance Energy Storage. *ACS Appl. Mater. Interfaces*. **15,** 52448–52460 (2023).
33. Zhang, Y., Jin, Y., Song, Y., Wang, H. & Jia, M. Induced bimetallic sulfide growth with reduced graphene oxide for high-performance sodium storage. *J. Colloid Interface Sci.* **642**, 554–564 (2023).
34. Anupama, B., Raguram, T. & Rajni, K. S. Synthesis and characterization of cobalt nickel oxide (CoNi2O4) prepared by one step hydrothermal method. *Mater. Today Proc.* **64**, 1694–1700 (2022).
35. Bhatt, M., Sinha, A. K., Bhojane, P., Singh, M. N. & Gupta, M. Structural and electronic properties of nickel–cobalt carbonate hydroxide hydrate nanostructures for high performance supercapacitor applications. *J. Mater. Sci. Mater. Electron.* **34**, 1933 (2023).
36. Bhat, K. S. & Nagaraja, H. S. Morphology-dependent electrochemical performances of nickel hydroxide nanostructures. *Bull. Mater. Sci.* **42**, 265 (2019).
37. Kumar, S., Satpathy, B. K. & Pradhan, D. Morphology-controlled synthesis of a NiCo-carbonate layered double hydroxide as an electrode material for solid-state asymmetric supercapacitors. Mater. Adv. **5,** 2271-2284 (2024).
38. Ranu, R. et al. Comparative microstructural analysis of V_2O_5 nanoparticles via x-ray diffraction (XRD) technique. *Nanotechnology* **35**, 435701 (2024).
39. Xu, X., Liu, W., Kim, Y. & Cho, J. Nanostructured transition metal sulfides for lithium ion batteries: Progress and challenges. *Nano Today*. **9**, 604–630 (2014).
40. Yu, K., Wang, J., Wang, X., Li, Y. & Liang, C. Zinc–cobalt bimetallic sulfide anchored on the surface of reduced graphene oxide used as anode for lithium ion battery. *J. Solid State Chem.* **290**, 121619 (2020).
41. Zu, L. et al. Mesoporous materials for Electrochemical Energy Storage and Conversion. *Adv. Energy Mater.* **10**, 2002152 (2020).
42. Isaacs, T. The mineralogy and chemistry of the nickel carbonates. *Mineral. Mag J. Mineral. Soc.* **33**, 663–678 (1963).
43. Pathak, A. K., Maity, D. K. & Distinctive IR Signature of $CO_3^{\bullet-}$ and CO_3^{2-} hydrated clusters: a theoretical study. *J. Phys. Chem. A*. **113**, 13443–13447 (2009).
44. Budipramana, Y., Ersam, T. & Kurniawan, F. Synthesis nickel hydroxide by electrolysis at high voltage. *ARPN J. Eng. Appl. Sci.* **9**, 2074–2077 (2014).
45. Du, H., Williams, C. T., Ebner, A. D. & Ritter, J. A. In situ FTIR spectroscopic analysis of carbonate transformations during adsorption and desorption of CO2 in K-promoted HTlc. *Chem. Mater.* **22**, 3519–3526 (2010).
46. Shabanian, M. et al. Novel nanocomposites consisting of a semi-crystalline polyamide and Mg–Al LDH: morphology, thermal properties and flame retardancy. *Appl. Clay Sci.* **90**, 101–108 (2014).
47. Price, E. A., Hammer, N. I. & Johnson, M. A. A cluster study of Cl2-Microhydration: size-dependent competition between symmetrical H-Bonding to the Anion and the formation of Cyclic Water networks in the Cl2-⊙ 1 – 5 (H2O) series. *J. Phys. Chem. A*. **108**, 3910–3915 (2004).
48. Karthick, K. et al. Cubic nanostructures of nickel–cobalt carbonate hydroxide hydrate as a high-performance oxygen evolution reaction Electrocatalyst in Alkaline and Near-Neutral Media. *Inorg. Chem.* **59**, 16690–16702 (2020).
49. Noman, M. et al. Sea urchin shaped hierarchical cobalt carbonate hydroxide hydrate-PANI nanocomposite with enhanced redox activity for asymmetric supercapacitor. *J. Energy Storage*. **73**, 109259 (2023).
50. Li, D. et al. Facile synthesis of Carbon Nanosphere/NiCo2O4 core-shell sub-microspheres for high performance Supercapacitor. *Sci. Rep.* **5**, 12903 (2015).
51. Bhojane, P. & Shirage, P. M. Impact of Post-synthesis heat treatment avoidance on cobalt carbonate hydroxide as a battery-type electrode material. *Appl. Surf. Sci.* **615**, 156352 (2023).
52. Chen, H. et al. Electrochemical conversion of $ni_2(OH)_2CO_3$ into $Ni(OH)_2$ hierarchical nanostructures loaded on a carbon nanotube paper with high electrochemical energy storage performance. *J. Mater. Chem. A*. **3**, 1875–1878 (2015).
53. Zou, Y. et al. Simple synthesis of core-shell structure of Co–Co3O4 @ carbon-nanotube-incorporated nitrogen-doped carbon for high-performance supercapacitor. *Electrochim. Acta*. **261**, 537–547 (2018).

54. Vijaya Sankar, K. & Kalai Selvan, R. Fabrication of flexible fiber supercapacitor using covalently grafted CoFe 2 O 4 /reduced graphene oxide/polyaniline and its electrochemical performances. *Electrochim. Acta*. **213**, 469–481 (2016).
55. Simonenko, T. L. et al. Synthesis and Printing features of a hierarchical nanocomposite based on nickel–cobalt LDH and carbonate hydroxide hydrate as a Supercapacitor Electrode. *Appl. Sci.* **13**, 5844 (2023).
56. Rajesh, J. A., Manikandan, R., Kim, J. Y. & Ahn, K. S. Engineering of binder-free cobalt carbonate hydroxide hydrate nanostructure for high-performance hybrid supercapacitors. *Electrochim. Acta*. **469**, 143293 (2023).
57. Tu, J. X. et al. Microwave hydrothermal electrodeposition of nickel carbonate hydroxide/cobalt hydroxide film on nickel foam for cement-based structural supercapacitors. *Mater. Today Chem.* **28**, 101365 (2023).
58. Cui, X. et al. Lawn-like cobalt carbonate hydroxide nanowire arrays induce the generation of oriented nickel/cobalt metal-organic framework for high performance supercapacitors. *J. Phys. Chem. Solids*. **193**, 112197 (2024).
59. Auti, P. S. et al. Hydrothermally synthesized MnCo2O4 nanoparticles for advanced energy storage applications. *Mater. Sci. Eng. B*. **301**, 117198 (2024).
60. Masikhwa, T. M. et al. Preparation and electrochemical investigation of the cobalt hydroxide carbonate/activated carbon nanocomposite for supercapacitor applications. *J. Phys. Chem. Solids*. **88**, 60–67 (2016).
61. Yewale, M. A. et al. Electrochemical study of CoV2O6 prepared by hydrothermal approach at different molar concentration of vanadium source. *Mater. Sci. Eng. B*. **307**, 117464 (2024).
62. Li, Y. et al. Unique 3D bilayer nanostructure basic cobalt carbonate@NiCo–layered double hydroxide nanosheets on carbon cloth for supercapacitor electrode material. *Ionics* **26**, 1397–1406 (2020).
63. Salunkhe, R. R., Jang, K., Lee, S. & Ahn, H. Aligned nickel-cobalt hydroxide nanorod arrays for electrochemical pseudocapacitor applications. *RSC Adv.* **2**, 3190 (2012).
64. Qiu, H. J., Peng, L., Li, X. & Wang, Y. Enhanced supercapacitor performance by fabricating hierarchical nanoporous nickel/nickel hydroxide structure. *Mater. Lett.* **158**, 366–369 (2015).
65. Tang, Y. et al. Morphology controlled synthesis of monodisperse cobalt hydroxide for supercapacitor with high performance and long cycle life. *J. Power Sources*. **256**, 160–169 (2014).
66. Xu, J., Gao, L., Cao, J., Wang, W. & Chen, Z. Preparation and electrochemical capacitance of cobalt oxide (Co3O4) nanotubes as supercapacitor material. *Electrochim. Acta*. **56**, 732–736 (2010).
67. Azizi, S., Seifi, M. & Askari, M. B. CoMoO4 as Pseudocapacitor Electrode Material and methanol Electro-Oxidation Catalyst. *J. Clust Sci.* **34**, 1727–1734 (2023).
68. Azizi, S. et al. MnCo2O4/activated carbon wheat husk (ACWH) as a novel electrode material for electrochemical capacitors. *Diam. Relat. Mater.* **137**, 110061 (2023).
69. Azizi, S., Askari, M. B., Rozati, S. M. & Masoumnezhad, M. Nickel ferrite coated on carbon felt for asymmetric supercapacitor. *Chem. Phys. Impact*. **8**, 100543 (2024).
70. Kandalkar, S. G., Gunjakar, J. L. & Lokhande, C. D. Preparation of cobalt oxide thin films and its use in supercapacitor application. *Appl. Surf. Sci.* **254**, 5540–5544 (2008).
71. Gao, Y., Chen, S., Cao, D., Wang, G. & Yin, J. Electrochemical capacitance of Co3O4 nanowire arrays supported on nickel foam. *J. Power Sources*. **195**, 1757–1760 (2010).
72. Khalaj, M., Sedghi, A., Miankushki, H. N. & Golkhatmi, S. Z. Synthesis of novel graphene/Co3O4/polypyrrole ternary nanocomposites as electrochemically enhanced supercapacitor electrodes. *Energy* **188**, 116088 (2019).
73. Liu, T. et al. Magnetic-field-assisted preparation of one-dimensional (1-D) wire-like NiO/Co3O4 composite for improved specific capacitance and cycle ability. *Mater. Lett.* **139**, 208–211 (2015).
74. Zhu, Y. et al. Large-scale synthesis of uniform NiCo2O4 nanoparticles with supercapacitive properties. *Mater. Lett.* **160**, 171–174 (2015).
75. Xiao, J. & Yang, S. Sequential crystallization of sea urchin-like bimetallic (Ni, Co) carbonate hydroxide and its morphology conserved conversion to porous NiCo2O4 spinel for pseudocapacitors. *RSC Adv.* **1**, 588 (2011).
76. Zhang, J., Liu, F., Cheng, J. P. & Zhang, X. B. Binary nickel–cobalt Oxides Electrode materials for high-performance supercapacitors: influence of its composition and porous nature. *ACS Appl. Mater. Interfaces*. **7**, 17630–17640 (2015).
77. Chang, J., Sun, J., Xu, C., Xu, H. & Gao, L. Template-free approach to synthesize hierarchical porous nickel cobalt oxides for supercapacitors. *Nanoscale* **4**, 6786 (2012).
78. Wan, L. et al. FeCoP nanosheets@Ni-Co carbonate hydroxide nanoneedles as free-standing electrode material for hybrid supercapacitors. *Chem. Eng. J.* **415**, 128995 (2021).
79. Isacfranklin, M. et al. CuCoO2 electrodes for supercapacitor applications. *Mater. Lett.* **296**, 129930 (2021).
80. Yewale, M. A. et al. Ni3V2O8 marigold structures with rGO coating for enhanced Supercapacitor Performance. *Micromachines* **15**, 930 (2024).

Acknowledgements

Authors acknowledge CIC, UPES, Dehradun, for providing the research facility. Archna Sagdeo at beam-line (BL-12), RRCAT, Indore, for XRD measurements. The authors also extend their gratitude to Deeksha Rani (PhD Scholar), IIT Ropar, for her contribution in providing characterization facilities, specifically SEM and XPS. Special thanks to Kajal (PhD Scholar UPES) for her help during experiments.

Author contributions

Mohit Bhatt (MB) conceptualized the idea, performed the synthesis and experiments, conducted all characterizations and compiled the data. MB have written the original manuscript. Anil Kumar Sinha (AKS) supervised the work, and played a crucial role in reviewing, reframing, and refining the manuscript. Bhavana Gupta reviewed the manuscript and provided suggetions.

Declarations

Competing interests

The authors declare no competing interests.

Additional information

Correspondence and requests for materials should be addressed to M.B. or A.K.S.